

HIGH-RESOLUTION IMAGING OF CO OUTFLOWS IN OMC-2 AND OMC-3

JONATHAN P. WILLIAMS

Institute for Astronomy, 2680 Woodlawn Drive, Honolulu, HI 96822; jpw@ifa.hawaii.edu

R. L. PLAMBECK

Astronomy Department, University of California, Berkeley, CA 94720; rplambeck@astro.berkeley.edu

AND

MARK H. HEYER

Department of Astronomy, LGRT 619, University of Massachusetts, 710 North Pleasant Street, Amherst, MA 01003;
 heyer@astro.umass.edu

Received 2003 January 20; accepted 2003 March 18

ABSTRACT

A large-scale, high-resolution map of CO (1–0) emission toward the OMC-2 and OMC-3 star-forming regions is presented. The map is a mosaic of 46 fields using the Berkeley-Illinois-Maryland Array (BIMA) and covers $\sim 10' \times 15'$ at $\sim 10''$ resolution. These data are combined with single-dish FCRAO observations and analyzed to identify and determine the properties of nine protostellar outflows. The BIMA data alone almost completely resolve out the cloud emission at central velocities and only recover 1/20 of the flux in the high-velocity gas, showing that outflows are generally broadly dispersed over $\sim 1'$ angular scales. All nine identified outflows emanate from known Class 0 or borderline Class 0/I sources, are associated with knots of shocked H₂ emission, and have short dynamical times. It is suggested that only the youngest, most spatially compact, and energetic outflows have been found and that more distributed high-velocity gas undetected by BIMA is due to older outflows continuing through the Class I phase of protostellar evolution. The mechanical energy injection rate into the cloud is estimated to be $\sim 1.5 L_{\odot}$, which is comparable to the turbulent energy dissipation rate. Outflows appear capable, therefore, of sustaining cloud turbulence but a high star formation rate is required, implying a short cloud lifetime of ≤ 5 Myr.

Subject headings: ISM: individual (OMC-2, OMC-3) — ISM: kinematics and dynamics — stars: formation — radio lines: ISM

On-line material: color figures

1. INTRODUCTION

The accretion of gas onto a protostar is accompanied by collimated jets observed in the optical and infrared (Mundt & Fried 1983; Schwartz et al. 1988) and swept-up molecular gas outflows observed at millimeter wavelengths (Snell, Loren, & Plambeck 1980). The resulting transfer of momentum and kinetic energy into a protostar's immediate surroundings may limit further accretion and thereby determine the final stellar mass (Shu, Adams, & Lizano 1987). The combined effect of multiple outflows averaged over space and time may also regulate future star formation on larger scales by maintaining cloud turbulence (McKee 1989). This paper addresses the latter issue by analyzing the energy injection rate into a cloud by a collection of very young outflows and the spatial distribution of high-velocity gas.

Molecular outflows are most powerful in the earliest, Class 0, stage of protostellar evolution (Bontemps et al. 1996). A chain of such young protostars was found by Chini et al. (1997, hereafter C97) through mapping dust continuum emission at $1300 \mu\text{m}$ along a ridge of dense molecular gas north of the Orion Nebula. Subsequent maps at $350 \mu\text{m}$ and $850 \mu\text{m}$ were made by Lis et al. (1998) and Johnstone & Bally (1999), respectively. The ridge is split into two main groups, OMC-2 in the southern half and OMC-3 in the north. The ratio of submillimeter to far-infrared luminosity is higher in OMC-3 than in OMC-2, suggesting a trend toward younger protostars with increasing distance from

the Orion Nebula (C97; Lis et al. 1998). However, all the sources found by C97 are deeply embedded and can be classified as either Class 0 or borderline Class 0/I. Other papers that are pertinent to this work are $2.12 \mu\text{m}$ imaging of the $\nu = 1-0$ S(1) line of shock excited H₂ by Yu, Bally, & Devine (1997, hereafter Y97) and, more recently, Stanke, McCaughrean, & Zinnecker (2002, hereafter S02). Y97 found 80 knots of H₂ emission, which they connected into 12 jets from young protostars. The positions of these knots are used as a guide to deciphering the molecular outflows in the maps presented here. S02 mapped a much larger region in Orion A and confirmed the positions of the Y97 knots in OMC2/3. Yu et al. (2000, hereafter Y00) followed up their H₂ imaging study with molecular line observations of several jets. C97 also presented molecular line observations. In both cases, the relatively large beam sizes ($>24''$) of these single-dish studies together with the high density of protostars and multiple, overlapping outflows prevented a firm association of molecular outflow gas with H₂ jets. Aso et al. (2000, hereafter A00) mapped CO (1–0) and denser gas tracers with the largest single-dish telescope operating at 3 mm, the Nobeyama 45 m, to achieve maps of the outflows at $17''$. They found eight outflows, and their map is the most comparable to this work.

Because of the high protostellar density in the region, it would be desirable to map the outflows at comparable resolution to the dust continuum maps that identified the young protostars. Only interferometers can achieve such a resolution, $\sim 10''$, in the low-frequency lines that the outflows

generally excite. The 10 6 m antennae that make up BIMA¹ provide excellent uv coverage and a large primary beam, which result in an efficient instrument for creating high-resolution, large-scale images of the millimeter sky. This paper presents a multifield BIMA mosaic of the CO (1–0) emission in the OMC2/3 region and shows the network of young molecular outflows from the clustered protostars in unprecedented detail. The following sections present the observational technique used to produce the map, general results from the data, and a description of each of the nine individual outflows that were identified. The paper concludes with a discussion of the implications of this work for outflow lifetimes, energetics, and cloud turbulence.

2. OBSERVATIONS

A 46 field mosaic was observed with BIMA four times from 1998 October to 1999 March, twice each in the compact C and D configurations. Baselines ranged from 6 to 81 m. The total on-source integration time was 14 hr, or slightly less than 20 minutes per field. Amplitude and phase were calibrated using 4 minute observations of 0530+135 interleaved with each 23 minute integration on source (30 s per field). Observations of the bright quasar 3C 454.3 at the start of each track showed the passband to be flat, and no correction was applied. The flux density scale was set by observing Mars during the 1998 observations resulting in a flux for 0530+135 of 2.0 Jy. The CO line was placed in the upper sideband centered in a 256 channel window with 25 MHz bandwidth with a corresponding velocity resolution of 0.25 km s^{-1} . The total continuum bandwidth was 600 MHz, but the integration time per field was too short to obtain more than a noisy detection of the brightest sources in the C97 map. The data were reduced in the MIRIAD software package (Wright & Sault 1993) and the final CLEANed map had a spatial resolution of $13''.4 \times 8''.8$ at a position angle of $1''.9$ and a (boxcar-smoothed) velocity resolution of 0.5 km s^{-1} . The final map covers $\sim 10' \times 15'$ at a spatial dynamic range $A_{\text{map}}/A_{\text{beam}} = 5800$.

The 46 pointing centers were arranged in a hexagonal grid spaced by $\Delta\alpha = 50''$, $\Delta\delta = 86''$. This resulted in a separation between pointing centers of $100''$, about the same as the primary beam of the 6 m antennae. Such a beam-sampled mosaic is sensitive to compact structures and is suited to mapping large areas with minimal observing overhead. A comparison between a beam-sampled and Nyquist-sampled mosaic of CO outflows in NGC 1333 showed negligible differences (Plambeck & Engargiola 2000). The noise level, 0.6 K (1σ) per 0.5 km s^{-1} velocity channel, was nearly uniform across the final map with a sharp falloff in sensitivity from 80% to 30% over $30''$ at the map borders.

Single-dish data were taken at the Five College Radio Astronomy Observatory 14 m telescope (FCRAO)² in 1999 March with the 16 element, focal plane array SEQUOIA and a system of autocorrelation spectrometers at a spectral resolution of 78 kHz. The observing was carried out using standard position-switching procedures resulting in a

Nyquist-sampled map with an rms noise of 0.3 K per 0.5 km s^{-1} channel. Antenna temperatures were converted to fluxes using a gain of 44.5 Jy K^{-1} and added to the BIMA data to fill in the short spacing information missing from the interferometer map through joint maximum entropy deconvolution.

The addition of the single-dish data partially compensates for the spatial filtering properties of the interferometer and makes possible flux recovery of extended objects. Interferometers null out features that are uniform over angular sizes $\theta \sim f\lambda/b_{\text{min}} \simeq 90''f$, where $b_{\text{min}} = 6 \text{ m} = 2.3 \text{ k}\lambda$ is the shortest projected baseline separation and f is a factor that theoretical considerations suggest may be $\simeq \frac{1}{2}$ (Wilner & Welch 1994). However, simulations by Helfer et al. (2002) show that the nonlinear deconvolution process can effectively extrapolate structural information to larger values of f . Experience suggests that D-array observations are sensitive to angular sizes $\lesssim 60''$, i.e., $f = \frac{2}{3}$. Since the beam size of the FCRAO 14 m at 115 GHz is $47''$, the combined BIMA+FCRAO data set provides information on small-scale and large-scale structures but poorly represents features on angular scales in the range $\sim 60''$ – $95''$.

3. RESULTS

3.1. Overview

Average spectra over the mapped region for each of the two data sets are shown in Figure 1. In contrast to the

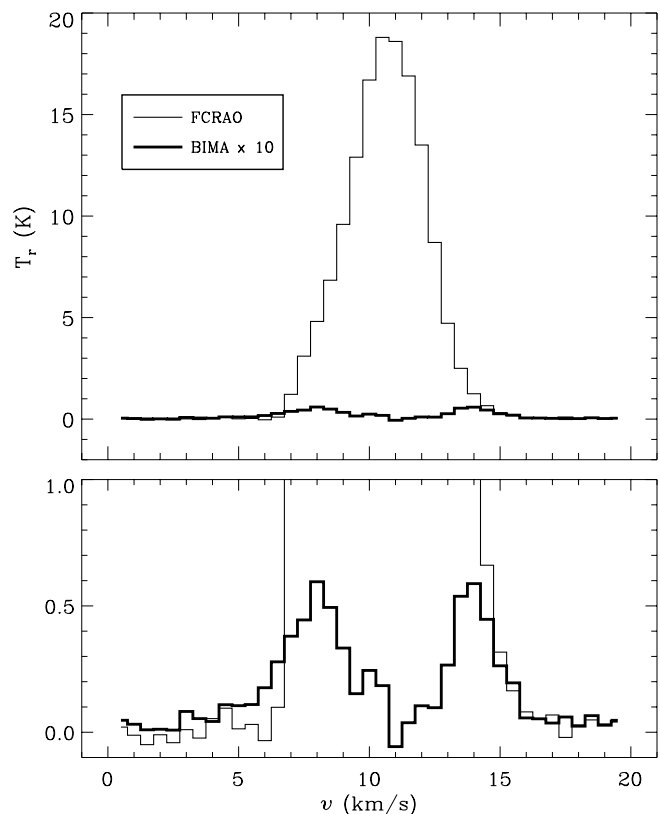


FIG. 1.—Average spectra over the entire mapped region for the FCRAO and BIMA data. The BIMA spectrum is scaled by a factor of 10 and plotted by heavy lines. The lower panel zooms in on the lower intensity emission and demonstrates that the interferometer data preferentially selects the high- and low-velocity gas from the small-scale features in outflows.

¹ Operated with support from the National Science Foundation under grants AST-9981308 to University of California, Berkeley, AST-9981363 to University of Illinois, and AST-9981289 to University of Maryland.

² FCRAO is supported in part by the National Science Foundation under grant AST-0100793 and is operated with permission of the Metropolitan District Commission, Commonwealth of Massachusetts.

single-dish map, large areas of the interferometer map have very little emission so the average intensity is much lower. Spectral profiles are also very different; the FCRAO spectrum is centrally peaked with weak extended line-wing emission, but the BIMA spectrum has a central dip and peaks in the line wings. This is due to the spatial filtering properties of interferometers as described above. In this case, it can be concluded that the bulk of the cloud emission at $v \simeq 9$ to 12.5 km s^{-1} is relatively smooth over angular scales $\gtrsim 1'$ but that the line-wing emission arises, at least in part, from more compact spatial features (i.e., collimated outflows). Similar single-dish/interferometer profiles were observed toward NGC 1333 and HH 7-11 by Plambeck & Engargiola (2000).

The BIMA data account for only 0.5% of the flux of the total cloud emission, as measured from the FCRAO data, demonstrating how smooth the CO emission is. Even in the line wings, however, the BIMA data only account for 4.7% of the emission, so a large fraction of the outflow emission must also be spatially extended over $\sim 1'$ angular scales. For this reason, outflow properties are calculated from the combined BIMA+FCRAO data set that contains the flux of the single-dish map. The broad spatial extent of the high-

velocity gas has important implications on its origin: either outflows can rapidly distribute their momenta and energy over large regions or most of the line-wing emission arises from a cascade of larger scale processes such as Galactic shear (Fleck 1981).

Although the BIMA data account for only $\sim 1/20$ of the flux of the line-wing emission, the spatial filtering properties of the interferometer are advantageous in isolating the small-scale features of collimated outflows. Low- and high-velocity BIMA emission is plotted in Figure 2. Several linear features can be seen and some clear outflows, MMS 5 and MMS 10 being the best examples, with separated blue-red lobes are apparent. Nine outflows were found in these data, and they are shown schematically in the map. All appear to originate from one of the C97 protostars. The Y97 H_2 knots are also plotted in the figure and were an essential guide in the assignment of the line-wing emission to different outflows. Most H_2 knots were found to be associated with CO line-wing emission, and those that were not appear to be due to outflows in the plane of the sky. Similarly, most of the CO features in Figure 2 can be assigned to an outflow

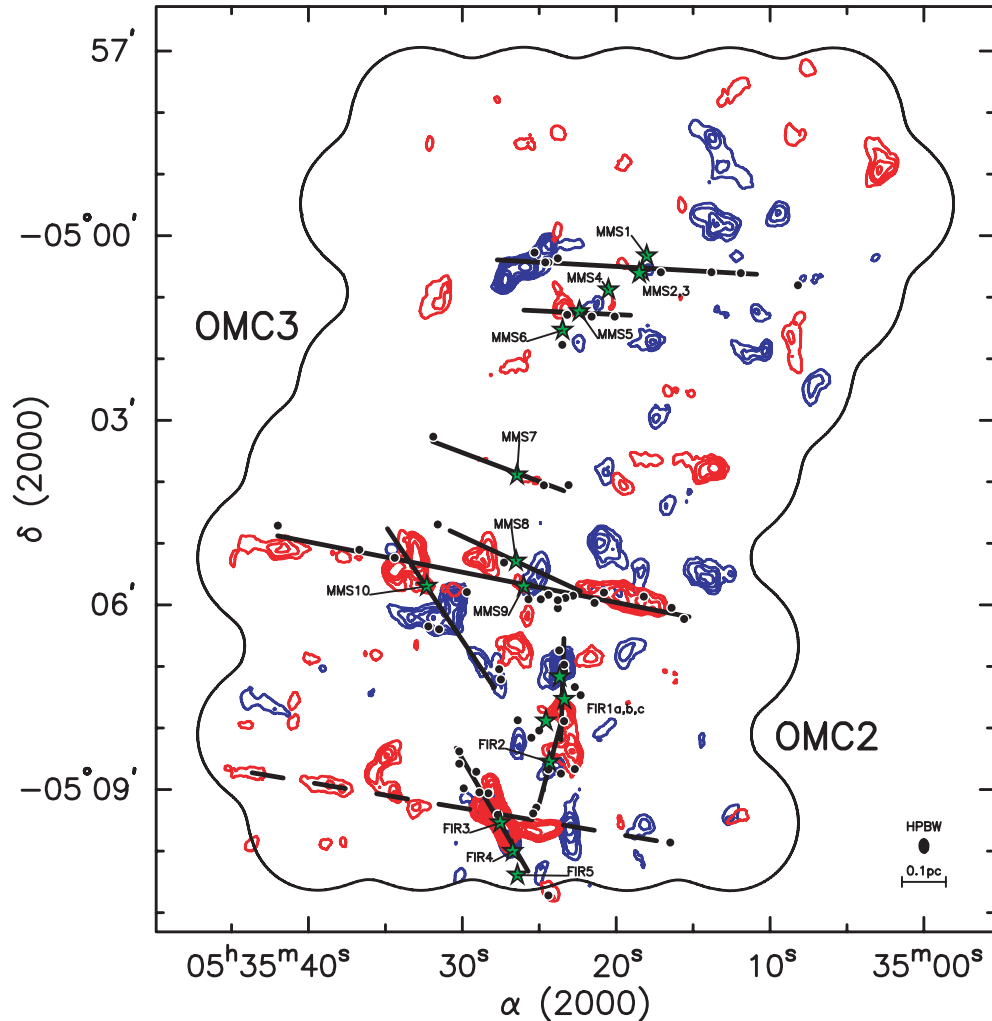


FIG. 2.—Line-wing emission from the BIMA mosaicked map (interferometer data only). Blue and red contours show the emission integrated from $v = 5.5$ to 9.0 km s^{-1} and 12.5 to 16.0 km s^{-1} , respectively. Contour starting levels and increments are the same ($8, 4 \text{ K km s}^{-1}$) for both velocity ranges. The labeled star symbols show the location of the C97 protostars and dots show the position of the Y97 $2.12 \mu\text{m}$ H_2 knots. Heavy dark lines show the outflows that are discussed in this paper. The solid contour outlining the map is the 30% sensitivity level of the mosaic. The $8'' \times 13''$ beam is plotted in the lower right corner.

from a C97 protostar, but there are also many clumps of high-velocity gas whose origin remains unclear.

3.2. Individual Flows

The identification of each of the nine outflows was made from analysis of channel maps and position-velocity slices in conjunction with the positions of the Y97 and S02 H₂ knots. Physical properties are listed in Table 1³ ordered by the C97 driving source, where MMS stands for “millimeter source” and FIR for “far-infrared.” For each outflow the mass, momentum, and energy were determined by first outlining the extent of the blue and red lobes in position and velocity space using interactive cursor-based IDL routines and then employing equations (6) and (9) of Cabrit & Bertout (1990). The combined BIMA+FCRAO data set was used for the calculations and, following Y00, CO line-wing emission was taken to be optically thin and at an excitation temperature of 30 K. Eyeball estimates of sizes and velocity gradients were made from the channel maps and position-velocity slices shown in Figures 3–7.

MMS 2/3.—This east-west outflow runs close to the plane of the sky (Fig. 3). There is a very weak red lobe coin-

cident with a string of H₂ knots and a compact blue lobe host to a cluster of H₂ knots. Because of its orientation, this outflow is one of the longest identified in these maps, and only a very slight velocity gradient could be measured across it. MMS 2 and MMS 3 are too close to unambiguously identify one over the other as the driving source of this flow. A large clump of high-velocity gas lies to the west that may be an expanding shell or loosely collimated outflow from any of MMS 2/3, 4, 5, or 6, but it is not associated with H₂ emission and could not be conclusively connected to any source.

MMS 5.—This is a small east-west outflow with blue and red peaks straddling MMS 5 along the same direction as a line of three H₂ knots (Fig. 3). The position-velocity map (Fig. 7) along this line shows the second highest velocity gradient measured out of the nine flows and suggests a near pole-on orientation. Two additional H₂ knots point to a north-south jet from MMS 6 (see also S02), but the CO emission is too confused in this area to definitively identify the corresponding outflow.

MMS 7.—Also known as IRAS 05329–0505, this source powers a bright reflection nebula and drives a well-collimated, one-sided (west) optical jet HH 294 (Reipurth, Bally, & Devine 1997). Y97 found a lone H₂ knot $\sim 2'$ to the east that they suggested was the end of a long flow from FIR 1c. The data here suggest that this knot is in fact associated with MMS 7 through a CO filament that appears to be an

³ A distance to the cloud of 450 pc is assumed (Brown, de Geus, & de Zeeuw 1994).

TABLE 1
OUTFLOW PROPERTIES

Region	M (M_{\odot})	P ($M_{\odot} \text{ km s}^{-1}$)	E (10^{43} ergs)	L (pc)	dV/dR ($\text{km s}^{-1} \text{ pc}^{-1}$)
MMS 2/3:					
Blue lobe	0.13	0.38	1.26		
Red lobe	0.08	0.24	0.78		
Total	0.21	0.62	2.04	0.54	21
MMS 5:					
Blue lobe	0.03	0.10	0.40		
Red lobe	0.02	0.09	0.34		
Total	0.05	0.19	0.74	0.13	100
MMS 7:					
Plane of sky	0.04			0.38	
MMS 8:					
Blue lobe	0.02	0.07	0.23		
Red lobe	0.04	0.13	0.44		
Total	0.06	0.20	0.67	0.20	55
MMS 9:					
Plane of sky	0.22			0.87	
MMS 10:					
Blue lobe	0.16	0.55	2.08		
Red lobe	0.14	0.49	2.04		
Total	0.30	1.04	4.12	0.39	34
FIR 1b/c:					
Blue lobe	0.11	0.28	0.79		
Red lobe	0.05	0.16	0.52		
Total	0.16	0.44	1.31	0.16	66
FIR 2:					
Blue lobe	0.02	0.08	0.29		
Red lobe	0.03	0.10	0.39		
Total	0.05	0.18	0.68	0.08	190
FIR 3: ^a					
Blue lobe	0.12	0.42	1.67		
Red lobe	0.21	0.74	3.32		
Total	0.33	1.16	4.99	0.27	66

^a Appears to be the sum of two overlapping flows.

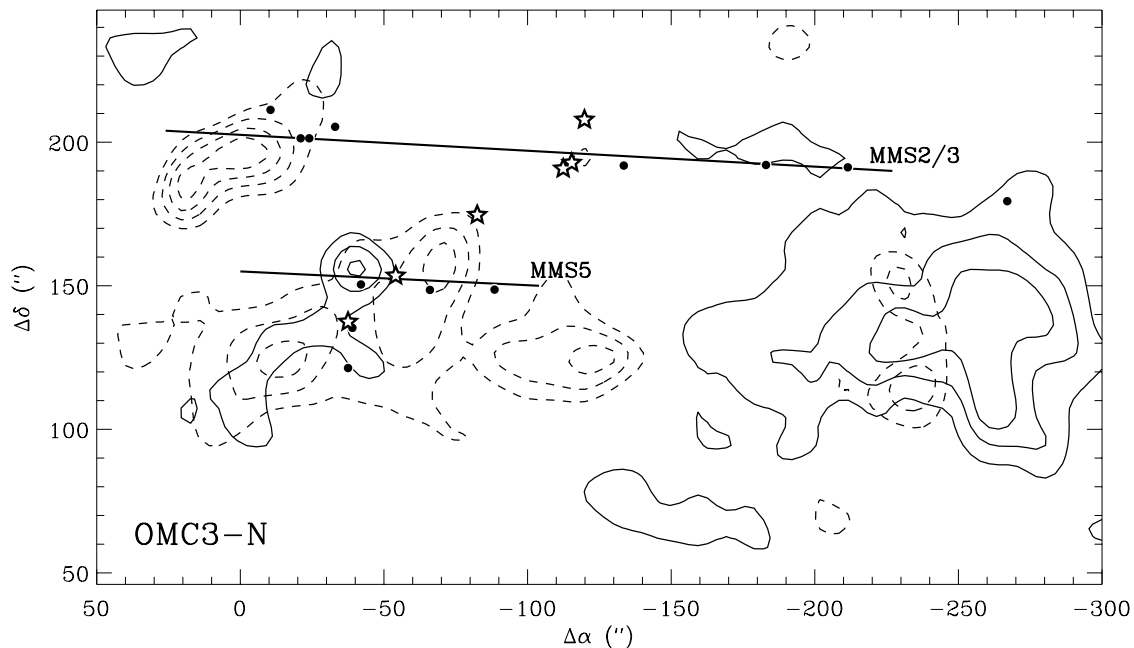


FIG. 3.—Line-wing emission from the combined BIMA+FCRAO mosaicked map toward the northern OMC-3 region containing sources MMS 1–6. Coordinates are offset from $\alpha = 5^{\text{h}}35^{\text{m}}26^{\text{s}}$ and $\delta = -5^{\circ}03'47''.7$ (J2000). The dashed contours show the low velocity gas integrated from $v = 5.0$ to 7.5 km s^{-1} , and solid contours the high-velocity gas integrated from $v = 13.5$ to 16.5 km s^{-1} . Contour starting levels and increments are the same ($8, 4 \text{ K km s}^{-1}$) for both velocity ranges. As in Fig. 2, the star symbols show the location of the C97 protostars and dots show the position of the Y97 $2.12 \mu\text{m}$ H_2 knots. The labeled heavy solid lines show the outflows that are discussed in this paper and along which the position-velocity maps are defined in Fig. 7. [See the electronic edition of the Journal for a color version of this figure.]

outflow in the plane of the sky (Fig. 4). The line-wing map in Figure 2 shows no high-velocity gas associated with MMS 7, but careful inspection of channel maps revealed a linear feature connecting the H_2 emission in HH 294 with the eastern knot. This putative outflow is just distinguish-

able above a broad plateau of cloud emission in a small range of velocities near the systemic motion of the cloud. Its direction is slightly different from the HH 294 optical jet but agrees with the position angle of a small 3.6 cm radio jet observed with the VLA (B. Reipurth et al. 2003, in

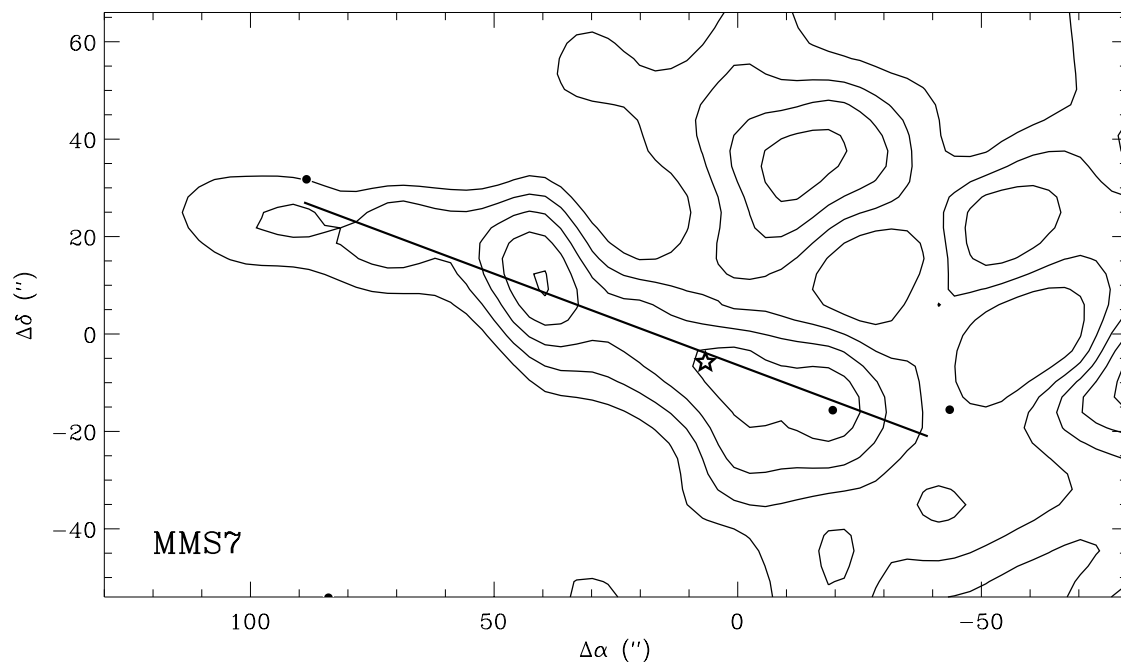


FIG. 4.—Contours of BIMA+FCRAO integrated emission from $v = 11.5$ to 13.5 km s^{-1} in the region around MMS 7. Because the velocity of this flow is similar to that of the bulk of the cloud emission, the total emission is very strong and contouring begins at 33 K km s^{-1} . The contour step is 3 K km s^{-1} . The solid dark line schematically marks the position of this flow, but no velocity gradient across it could be reliably measured. [See the electronic edition of the Journal for a color version of this figure.]

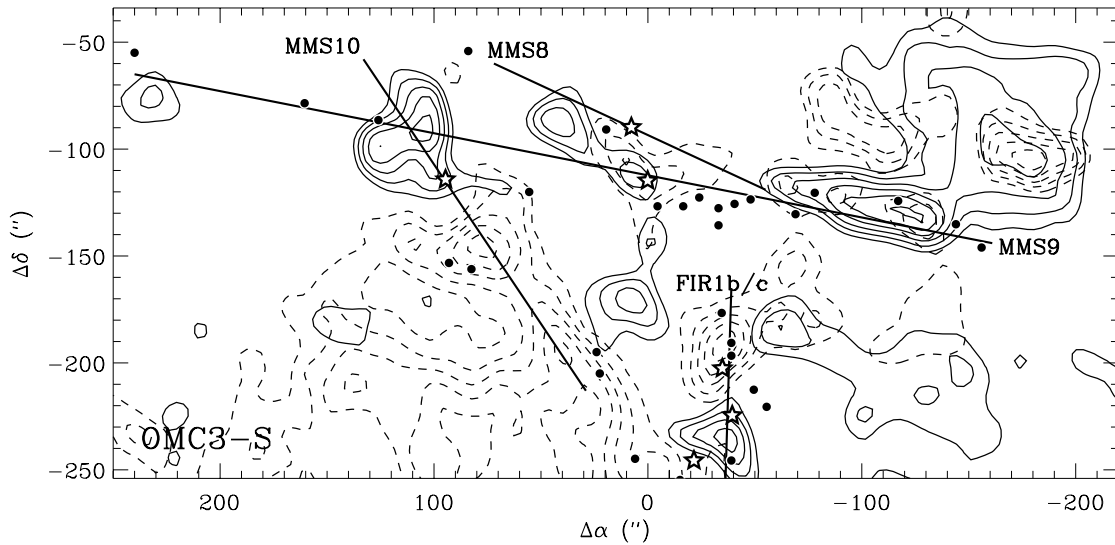


FIG. 5.—Same as Fig. 3, but for the southern part of OMC-3 containing sources MMS 8–10. Dashed contours are for $v = 4.0$ to 8.0 km s^{-1} and solid contours are for $v = 13.0$ to 16.0 km s^{-1} . Contours begin at 12 K km s^{-1} and increment at 4 K km s^{-1} . [See the electronic edition of the *Journal* for a color version of this figure.]

preparation). Because of its orientation in the plane of the sky and immersion in the general cloud emission, no velocity gradient could be measured along the flow and only conservative estimates to its size and mass could be made.

MMS 8.—The identification of this flow is the most uncertain of the nine. Channel maps and position-velocity cuts hint at an outflow around MMS 8 that connects several Y97 H_2 knots (Fig. 5), but there is confusion from high-velocity CO emission around MMS 9 and the dense chain of H_2 knots from the well-collimated

jet that it powers. As originally noted by Y00, the powerful CO outflow around MMS 8 discussed in C97 was misidentified due to erroneous plotting of source positions and is a combination of flows originating from MMS 9 and MMS 10.

MMS 9.—A prominent chain of H_2 knots reveal a long east-west jet originating from MMS 9 (Y97; S02). The BIMA data show associated, collimated, high-velocity $v > 13 \text{ km s}^{-1}$ CO (Fig. 5). On the eastern side of the source, the association of both H_2 knots and gas is less clear, but a

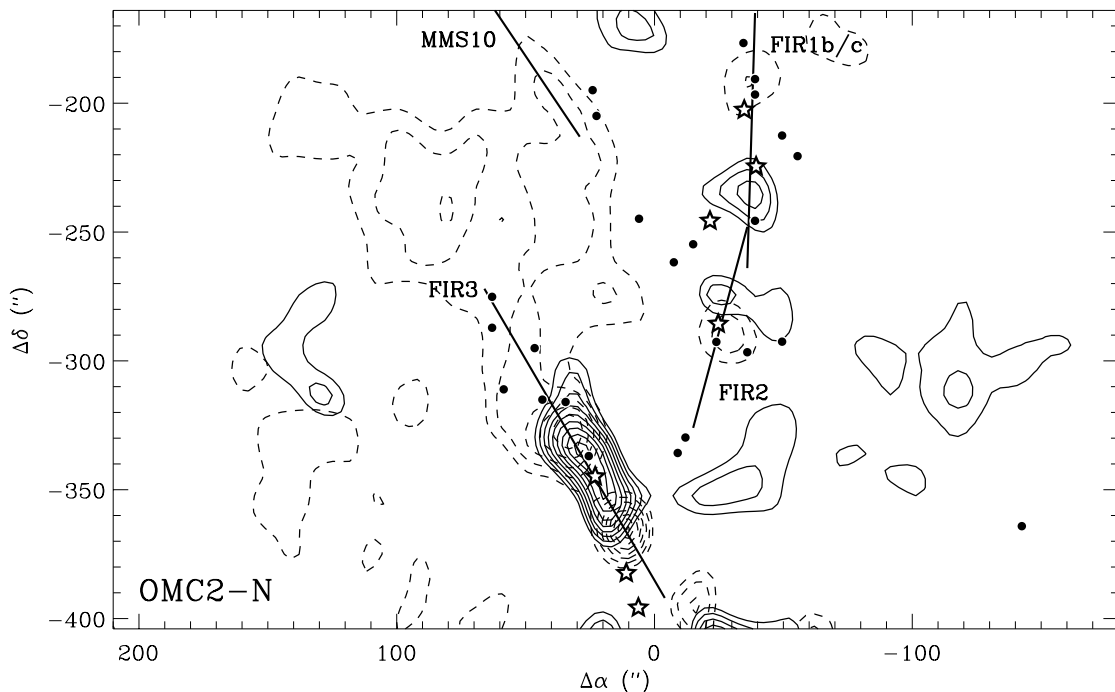


FIG. 6.—Same as Fig. 3, but for the northern part of OMC-2 containing sources FIR 1–6. Dashed contours are for $v = 4.0$ to 7.5 km s^{-1} and solid contours are for $v = 13.5$ to 17.0 km s^{-1} . Contours begin at 12 K km s^{-1} and increment at 4 K km s^{-1} . [See the electronic edition of the *Journal* for a color version of this figure.]

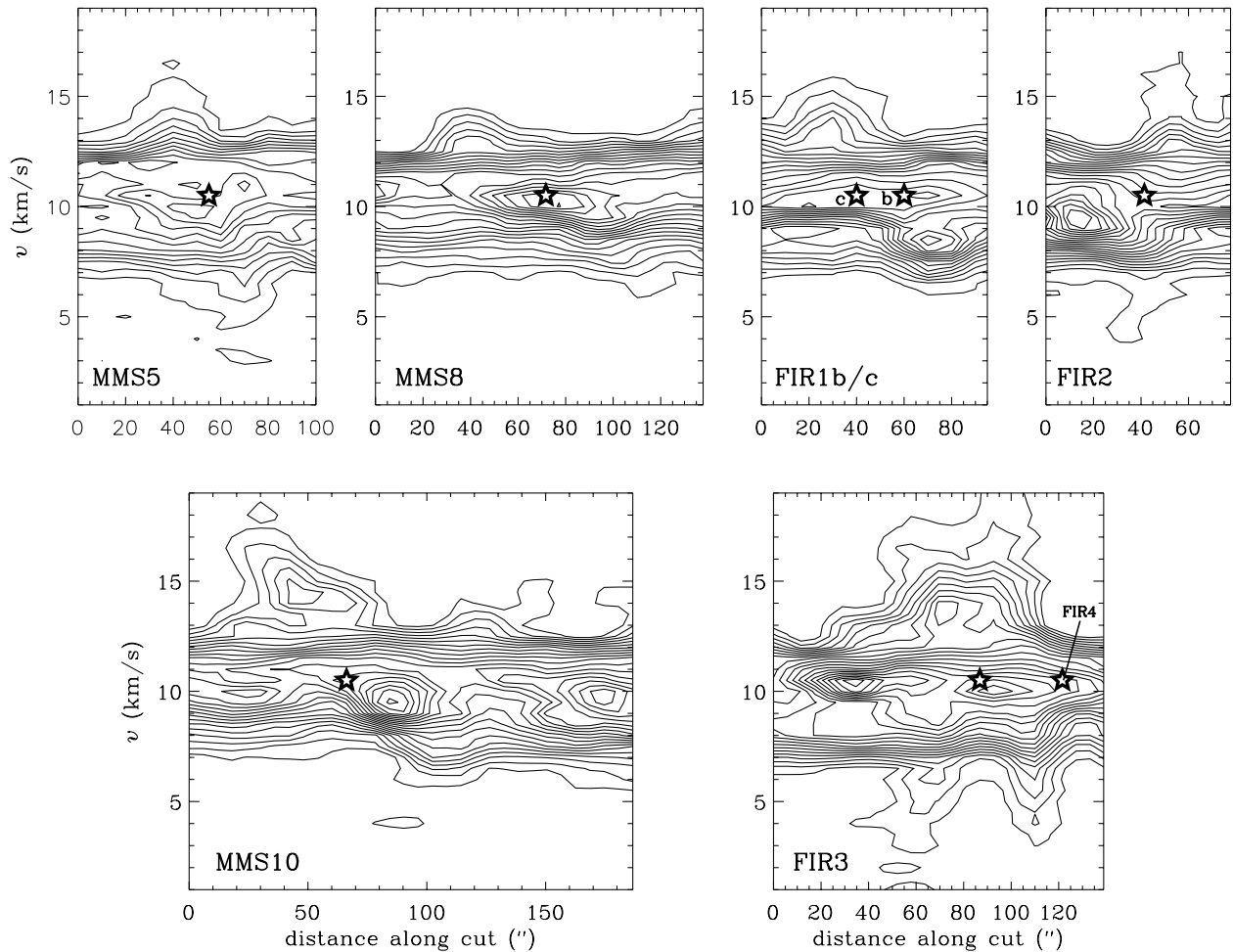


FIG. 7.—Position-velocity maps along the cuts defined in Figs. 3, 5, and 6. The position increases from the leftmost (east) portion of the cut in each case. The long outflows from MMS 2/3 and MMS 9 that lie predominantly along the plane of the sky have low velocity gradients and are not shown. The contour starting level and increment are 2 K for all maps. The locations of the Chini et al. protostars along the cut (at an assumed $v = 10.5 \text{ km s}^{-1}$) are shown by the star symbols and labeled in the two cases in which more than one source lies along the cut.

long, high-velocity collimated flow is discernible and best seen in Figure 2. The flow occurs over a narrow range of velocities and suggests an orientation in the plane of the sky, consistent with its projected length, almost 1 pc, by far the longest of the nine flows in Table 1.

Two compact cores of low-velocity gas lie to the west of MMS 9 and were connected to the high-velocity core north of MMS 10 by both Y00 and A00. However, the greater resolution of these data clearly demonstrate that the H_2 jet is associated with the linear high-velocity core $\sim 30''$ farther south. A more diffuse red lobe is also found toward the blue cores which suggests that this feature may be a pole on flow from an unidentified source or an expanding shell from an older outflow.

MMS 10.—This is a strong, clearly defined outflow running northeast-southwest (Fig. 5). Y00 suggest that the red lobe here is due to the outflow from MMS 9. While there is likely to be some contribution from that flow, the higher resolution of these data shows a clear relationship in space and velocity (Fig. 7) between MMS 10 and the strong blue and red lobes on either side of it. The H_2 knots appear to be associated with the edges of the CO lobes rather than directly lining up with a single jet from the source itself. This is one of the more massive flows identified in the cloud.

FIR 1b/c.—This outflow occurs in a highly confused area of the maps where the source density is high and there are multiple, overlapping flows. Because of the large numbers of high-velocity CO clumps and scattered H_2 knots here, the identification of this outflow is uncertain. The evidence for an outflow is based on the blue and neighboring red lobes on either side of FIR 1c and FIR 1b and H_2 knots in close, but not exact, proximity (Figs. 5 and 6). A position-velocity cut along a line through the two sources is unable to distinguish one over the other as the driving source (Fig. 7).

FIR 2.—This is a very weak but high-velocity flow running north-south. The two lobes almost overlap spatially (Fig. 6) but extend over a wide range in velocity (Fig. 7) resulting in an extremely high velocity gradient and suggesting a pole-on orientation. H_2 knots are found in the vicinity of FIR 2, but their association with this flow is uncertain and they may well be an extension of the powerful MMS 10 outflow.

FIR 3.—A compact chain of H_2 knots and intense, collimated, high-velocity CO emission reveal strong outflow activity. This source is a binary with $4''$ separation (Pendleton et al. 1986) and appears to drive two criss-crossed flows. Channel maps show two blue lobes and a single, long, red lobe (Fig. 6). The position-velocity map in

Figure 7 shows the two blue lobes more clearly. Their red lobe counterparts can be seen in the two lowest contour levels of the merged high-velocity emission in the same figure. The sum of these two flows inject the most mass, momentum, and energy into the cloud of the nine flows discussed in this work.

In addition, a potential tenth flow is seen in the BIMA map (Fig. 2, *dashed line*). This connects a single H₂ knot in the southwest with a chain of high-velocity clumps that appear to connect back to FIR 3. It was, however, not possible to distinguish this flow clearly in the combined BIMA+FCRAO data set because of its length, lack of strong velocity gradient, and the confusion of background cloud emission.

4. DISCUSSION

The OMC-2 and OMC-3 regions are highly active star-forming centers with multiple, overlapping outflows. High-resolution, large-scale CO mapping allows more secure identification of the flows and their driving sources and makes possible the determination of fundamental physical properties such as mass, momentum, and energy. In practice, low and high-velocity clumps are found to be widely distributed across the map and, particularly for the flows in the plane of the sky, it was essential to use the Y97 and S02 H₂ maps to assign these features to outflows driven by a given source.

The nine identified CO outflows line up with ~ 50 of the 60 Y97 H₂ knots in the mapped region. There were no clearly identifiable bipolar CO outflows that were not associated with detectable molecular hydrogen shocks. This is partly, but not completely, due to the way in which the high-velocity gas is assigned to outflows. The additional information provided by the CO data, however, shows that the extremes of some of the jets found by Y97 appear to be misidentified. For example, in Y97 the H₂ knots 74/77, 76, and 79 define the ends of jets I, E, and J, respectively, but the CO data show that these knots are more likely to be associated with flows from closer submillimeter sources, MMS 10, MMS 7, and either MMS 9 or MMS 10, respectively. These jets are likely, therefore, to be significantly smaller than previously thought. On the other hand, the MMS 2/3 and MMS 9 flows that lie in the plane of the sky appear to have a measurable effect on the CO emission over a sizeable fraction of a parsec in length, as has been well established for optical jets (Reipurth & Bally 2001).

The large-scale effect of outflows may also be apparent in the “missing flux” in the BIMA map because of structures that are larger than $\sim 1'$. Over 95% of the line-wing emission is resolved out by the interferometer, demonstrating that the high-velocity gas is broadly distributed. Similarly, a map of the CO line width at $10''$ resolution made from the combined data set is generally featureless across the cloud away from a few peaks toward individual sources, such as FIR 3 and some H₂ knots along the MMS 9 flow.

The fact that the line-wing emission is widely distributed complicates the definition of the boundaries of the outflows and the measurement of their physical properties. Additional uncertainties are the optical depth of the CO line-wing emission and the inclination of the flow to our line of sight. Since there are no ¹³CO observations at the same resolution, optically thin emission was assumed, providing a lower limit to the mass and kinematic estimates. No inclination correction was applied to the individual flow momenta

and energies listed in Table 1, since it is difficult to determine accurately. Assuming, however, a mean inclination of 45° for the outflow sample, total values of the mass, momentum, and energy are $1.4 M_\odot$, $5.4 M_\odot \text{ km s}^{-1}$, and 2.9×10^{44} ergs, respectively. The variation in masses of individual outflows is about a factor of 5, but the velocities do not greatly differ and the range of momenta and energies is only a factor of 6. There is no clear correlation between outflow properties and the C97 driving source mass or luminosity.

Velocity gradients, $dV/dR \simeq (V_{\text{red}} - V_{\text{blue}})/L$, measured by eyeball fits to the position-velocity diagrams in Figure 7, are given in Table 1. Velocity gradients for the two long outflows from MMS 2/3 and MMS 9 that lie nearly in the plane of the sky could not be accurately measured. The inverse of the gradient in $\text{km s}^{-1} \text{ pc}^{-1}$ is approximately the dynamical time in Myr. The median dynamical time in this sample is 2×10^4 yr, which is similar to the statistical lifetime of Class 0 protostars in the ρ Oph cluster (André & Montmerle 1994). However, the identification of the outflows here suffers from a bias toward either high velocity gradients or sharp, collimated features that stand out against the general cloud emission. The former corresponds to short dynamical timescales and the latter is a probable indication of youth (Masson & Chernin 1993). It is not necessarily surprising, then, that all nine flows described in this paper appear to be driven by a young Class 0, or borderline Class 0/I, protostar in the C97 catalog.

The dynamical time is only a lower limit to the age of an outflow (Parker, Padman, & Scott 1991) but is probably a good estimator for the young outflows observed here (Masson & Chernin 1993). If only the very youngest outflows, $t_{\text{flow}} \sim 2 \times 10^4$ yr, have been identified, but (less well collimated) outflow activity continues throughout the Class I phase, $t_1 \sim \text{few} \times 10^5$ yr (Wilking, Lada, & Young 1989), then the broadly distributed line-wing emission that was resolved out in the BIMA map can be accounted for by outflows alone. In principle, they should be apparent in a combined single-dish+interferometer map such as the one presented in this paper, but data with a higher signal-to-noise ratio are required to pick them out from the general cloud background. This paper has focused on the high-velocity gas that can be identified with shocked H₂ emission, but there are several other high-velocity clumps in Figure 2 that were not associated with outflows. These unassigned clumps may be parts of older outflow shells that have broadened and slowed sufficiently such that the shocks with the ambient medium are too weak to excite the H₂ 2.12 μm line. Earlier single-dish maps of CO in Orion indeed found several large-scale, slowly expanding shells that were interpreted as resulting from young stellar outflows (Heyer et al. 1992).

It has long been suggested that outflows can maintain cloud turbulence (e.g., Norman & Silk 1980). The agreement between the ratio of Class 0 to Class I lifetimes, and the flux ratio between collimated and broad outflows imply that the more powerful but short-lived Class 0 outflows inject a similar amount of energy into the cloud as the slower but more numerous Class I outflows. The total energy input into the cloud is therefore,

$$\begin{aligned} L_{\text{flow}} &= \frac{E_{\text{flow}}}{t_{\text{flow}}} \Big|_{\text{Class 0}} + \frac{E_{\text{flow}}}{t_{\text{flow}}} \Big|_{\text{Class I}} \simeq 2 \frac{E_{\text{flow}}}{t_{\text{flow}}} \Big|_{\text{Class 0}} \\ &= \frac{2 \times 2.9 \times 10^{44} f_{\text{CO}} \text{ ergs}}{2 \times 10^4 \text{ yr}} \simeq 9 \times 10^{32} f_{\text{CO}} \text{ ergs s}^{-1}, \end{aligned}$$

where f_{CO} is a factor that corrects for the assumption of optically thin CO line-wing emission in the calculation of the outflow masses and energies. Cabrit & Bertout (1990) show that f_{CO} lies in the range 5–10. The cloud loses energy through turbulent decay. Simulations of magnetohydrodynamic cloud turbulence show rapid dissipation with a timescale

$$t_{\text{diss}} = \left(\frac{3.9\kappa}{M_{\text{rms}}} \right) t_{\text{ff}},$$

where $\kappa = \lambda_d/\lambda_J$ is the driving wavelength of the turbulence in units of the Jean's length, M_{rms} is the rms Mach number of the turbulence, and $t_{\text{ff}} = (3\pi/32G\rho)^{1/2}$ is the free-fall timescale (MacLow 1999). The mass of the OMC-2/3 complex is $1100 M_{\odot}$ (Lis et al. 1998). The average temperature and one-dimensional velocity dispersion can be measured from the FCRAO spectrum in Figure 1 and are equal to 20 K and 1.5 km s^{-1} , respectively. The equivalent radius, measured from the projected area, is 1.2 pc, and implies an average number density, $n_{\text{H}_2} = 2 \times 10^3 \text{ cm}^{-3}$. These numbers imply a total kinetic (turbulent) energy $E_{\text{turb}} = 7.4 \times 10^{46}$ ergs, Mach number $M_{\text{rms}} = 5$, and free-fall time $t_{\text{ff}} = 6 \times 10^5 \text{ yr}$. Parameterizing by κ , the dissipation time is $t_{\text{diss}} = 4.7 \times 10^6 \kappa \text{ yr}$, and the turbulent energy dissipation rate is

$$L_{\text{turb}} = \frac{E_{\text{turb}}}{t_{\text{diss}}} = 5 \times 10^{33} \kappa^{-1} \text{ ergs s}^{-1}.$$

The average cloud density and temperature imply a Jean's length $\lambda_J = 0.2 \text{ pc}$. If outflows sustain the turbulence, the driving wavelength can be no greater than their size

$\lambda_d \leq \langle L \rangle$. The average outflow length in Table 1, corrected for an average inclination angle of 45° , is $\langle L \rangle = 0.5 \text{ pc}$. Thus, $\kappa = \lambda_d/\lambda_J \leq 2.5$. Shorter wavelength “harmonics” may also be present, however, and MacLow (1999) argues that the driving wavelength must be less than the Jean's length, i.e., $\kappa < 1$, for turbulence to support the cloud. Taking $\kappa \simeq 1$ and a conservative CO optical depth correction $f_{\text{CO}} = 5$, the data are consistent with an approximate balance between outflow energy injection rate and turbulent energy dissipation rate,

$$L_{\text{flow}} \simeq L_{\text{turb}} \simeq 5 \times 10^{33} \text{ ergs s}^{-1} = 1.3 L_{\odot}.$$

To maintain the cloud turbulence over longer timescales than an individual protostar's outflow lifetime requires a star formation rate $\sim 9 \text{ stars}/2 \times 10^4 \text{ yr} \sim 2.3 \times 10^{-4} M_{\odot} \text{ yr}^{-1}$ for an average protostellar mass of $0.5 M_{\odot}$ based on the Scalo (1986) IMF. At this rate the OMC-2/3 complex has enough mass to continue forming low-mass stars for $5 \times 10^6 \text{ yr}$, where $\epsilon = M_{*,\text{tot}}/M_{\text{cloud}} < 1$ is the overall star formation efficiency. Even if the cloud ultimately converts most of its mass to stars, therefore, the high rate of turbulent energy dissipation restricts its lifetime to a few Myr. This is shorter than predicted for more massive GMCs (Blitz & Shu 1980; Williams & McKee 1997) but consistent with the rapid cloud formation and evolution scenario proposed by Hartmann, Ballesteros-Paredes, & Bergin (2001) and the observed small age spread of protostars in nearby star-forming regions (Hartmann 2001).

J. P. W. is supported by NSF grant AST-0134739 and thanks Bo Reipurth and Joan Najita for helpful discussions.

REFERENCES

- André, P., & Montmerle, T. 1994, *ApJ*, 420, 837
Aso, Y., Tatematsu, K., Sekimoto, Y., Nakano, T., Umemoto, T., Koyama, K., & Yamamoto, S. 2000, *ApJS*, 131, 465 (A00)
Blitz, L., & Shu, F. H. 1980, *ApJ*, 238, 148
Bontemps, S., André, P., Terebey, S., & Cabrit, S. 1996, *A&A*, 311, 858
Brown, A. G. A., de Geus, E. J., & de Zeeuw, P. T. 1994, *A&A*, 289, 101
Cabrit, S., & Bertout, C. 1990, *ApJ*, 348, 530
Chini, R., Reipurth, B., Ward-Thompson, D., Bally, J., Nyman, L.-A., Sievers, A., & Billawala, Y. 1997, *ApJ*, 474, L135 (C97)
Fleck, R. C. 1981, *ApJ*, 246, L151
Hartmann, L. 2001, *AJ*, 121, 1030
Hartmann, L., Ballesteros-Paredes, J., & Bergin, E. A. 2001, *ApJ*, 562, 852
Helfer, T. T., Vogel, S. N., Lugten, J. B., & Teuben, P. J. 2002, *PASP*, 114, 350
Heyer, M., Morgan, J., Schloerb, F. P., Snell, R. L., & Goldsmith, P. F. 1992, *ApJ*, 395, L99
Johnstone, D., & Bally, J. 1999, *ApJ*, 510, L49
Lis, D. C., Serabyn, E., Keene, J., Dowell, C. D., Benford, D. J., Phillips, T. G., Hunter, T. R., & Wang, N. 1998, *ApJ*, 509, 299
MacLow, M.-M. 1999, *ApJ*, 524, 169
Masson, C. R., & Chernin, L. M. 1993, *ApJ*, 414, 230
McKee, C. F. 1989, *ApJ*, 345, 782
Mundt, R., & Fried, J. W. 1983, *ApJ*, 274, L83
Norman, C., & Silk, J. 1980, *ApJ*, 238, 158
Parker, N. D., Padman, R., & Scott, P. F. 1991, *MNRAS*, 252, 442
Pendleton, Y., Werner, M. W., Capps, R., & Lester, D. 1986, *ApJ*, 311, 360
Plambeck, R. L., & Engargiola, G. 2000, in *ASP Conf. Ser. 217, Imaging at Radio through Submillimeter Wavelengths*, ed. J. G. Mangum & S. J. E. Radford (San Francisco: ASP), 354
Reipurth, B., & Bally, J. 2001, *ARA&A*, 39, 403
Reipurth, B., Bally, J., & Devine, D. 1997, *AJ*, 114, 2708
Scalo, J. 1986, *Fundam. Cosmic Phys.*, 11, 1
Schwartz, R. D., Jennings, D. G., Williams, P. M., & Cohen, M. 1988, *ApJ*, 334, L99
Shu, F. H., Adams, F. C., & Lizano, S. 1987, *ARA&A*, 25, 23
Snell, R. L., Loren, R. B., & Plambeck, R. L. 1980, *ApJ*, 239, L17
Stanke, T., McCaughrean, M. J., & Zinnecker, H. 2002, *A&A*, 392, 239 (S02)
Wilking, B. A., Lada, C. J., & Young, E. T. 1989, *ApJ*, 340, 823
Williams, J. P., & McKee, C. F. 1997, *ApJ*, 476, 166
Wilner, D. J., & Welch, W. J. 1994, *ApJ*, 427, 898
Wright, M. C. H., & Sault, R. J. 1993, *ApJ*, 402, 546
Yu, K., Bally, J., & Devine, D. 1997, *ApJ*, 485, L45 (Y97)
Yu, K., Billawala, Y., Smith, M. D., Bally, J., & Butner, H. M. 2000, *AJ*, 120, 1974 (Y00)